Dissipation and oscillatory solvation forces in confined liquids studied by small-amplitude atomic force spectroscopy

2010 Nanotechnology 21 325703

(http://iopscience.iop.org/0957-4484/21/32/325703)

Nanotechnology **21** (2010) 325703 (11pp) doi:10.1088/0957-4484/21/32/325703

Dissipation and oscillatory solvation forces in confined liquids studied by small-amplitude atomic force spectroscopy

Sissi de Beer, Dirk van den Ende and Frieder Mugele

Physics of Complex Fluids, Department of Science and Technology, University of Twente, PO Box 217, 7500 AE Enschede, Netherlands

E-mail: s.j.a.debeer@utwente.nl

Received 11 March 2010, in final form 6 June 2010
Published 19 July 2010
Online at stacks.iop.org/Nano/21/325703

Abstract

We determine conservative and dissipative tip–sample interaction forces from the amplitude and phase response of acoustically driven atomic force microscope (AFM) cantilevers using a non-polar model fluid (octamethylcyclotetrasiloxane, which displays strong molecular layering) and atomically flat surfaces of highly ordered pyrolytic graphite. Taking into account the base motion and the frequency-dependent added mass and hydrodynamic damping on the AFM cantilever, we develop a reliable force inversion procedure that allows for extracting tip–sample interaction forces for a wide range of drive frequencies. We systematically eliminate the effect of finite drive amplitudes. Dissipative tip–sample forces are consistent with the bulk viscosity down to a thickness of 2–3 nm. Dissipation measurements far below resonance, which we argue to be the most reliable, indicate the presence of peaks in the damping, corresponding to an enhanced 'effective' viscosity, upon expelling the last and second-last molecular layer.

S Online supplementary data available from stacks.iop.org/Nano/21/325703/mmedia

(Some figures in this article are in colour only in the electronic version)

1. Introduction

The properties of liquids confined between solid surfaces are crucial for understanding numerous technological problems including lubrication and nanotribology, porous media and nanofluidic devices for biotechnological applications [1]. The key question is to what extent macroscopic continuum physics—in particular hydrodynamics—can be applied to describe the systems at such small scales and, if not, how deviations from the macroscopic behaviour manifest themselves.

It is by now well established that the structure of the liquid is altered close to the solid–liquid interface in such a way that the liquid molecules assume a layer structure parallel to the interface. This gives rise to oscillations in the average density and to (conservative) oscillatory solvation forces upon confining the liquid between two solid surfaces [2]. In addition to this structuring, some studies also report a strongly increased dissipation and, in some cases, even solid-like friction for liquid films with a thickness of several molecular layers [3, 4]. In contrast, other studies find essentially bulk-like viscous dissipation, except for the molecular layers directly adjacent to the solid, which behave more rigidly [5, 6]. According to molecular simulations both solidification and liquid-like behaviour can be achieved, depending on the interaction potentials between the solid and the liquid. While most simulations focused on equilibrium properties and the resulting conservative forces, Gao and Landman [7] also reported that the diffusivity in confined liquids is maximum for surface separations corresponding to a non-integer number of molecular layers corresponding to states with a reduced density. The fluctuation–dissipation theorem—if applicable to these systems—then suggests periodic variations in the (viscous) dissipation for strongly layered liquids.

Do such periodic variations exist? A number of recent atomic force microscopy (AFM) experiments addressed this question using various measurement techniques, including conventional amplitude modulation (AM) AFM and frequency modulation (FM) AFM and different driving schemes (acoustic/base drive versus magnetic drive). While studies

using the acoustic scheme [8, 9] reported oscillations in the dissipation, a continuous increase by several orders of magnitude was reported in the magnetically driven systems [10, 11]. (Very recently a sharply peaked and periodic dissipation was also reported in a very careful experiment using the magnetic scheme [12].) Thus, even for simple (Lennard-Jones-like) model systems, such as the most widely used octamethylcyclotetrasiloxane (OMCTS), the question how confinement affects dissipation has yet to be answered.

From a technical perspective, the acoustic driving scheme in AFM is frequently criticized for its known sensitivity to experimental and modelling errors (see [13] in the present context). Yet, AFM cantilevers driven at sufficiently small amplitudes are known to behave as harmonic oscillators and are therefore in principle straightforward to model. This raises the important—given the dominance of acoustically driven AFMs—technical question under which conditions and to what extent reliable interaction forces can be extracted from AM-AFM measurements. Despite the fact that the relevance of taking into account the motion of the cantilever base has been known for a long time [14], it was noticed only recently [15] that the acoustic driving scheme gives rise to a particularly strong phase response at *low* driving frequencies, which offers the potential of an increased sensitivity.

In this paper we elaborate on our work which was presented earlier in [15]. While in [15] we presented a model to describe the cantilever dynamics, we now address both the technical question of obtaining reliable tip–sample interaction forces from small-amplitude (AM)-AFM measurements and the physical question regarding the effect of confinement on the stiffness and dissipation in confined layers of OMCTS. To do so, we measure and model the response curve of the AFM cantilever as a function of the drive frequency incorporating (in addition to the motion of the cantilever base which was already discussed in [15]) the frequency-dependent added mass and dissipation around the cantilever. Subsequently, we measure the amplitude–phase-distance (APD) curves over a wide range of driving frequencies and extract the corresponding conservative and dissipative tip–sample interaction forces. Eliminating the effect of finite drive amplitudes, we obtain consistent conservative tip–sample interactions over the entire range of drive frequencies. The corresponding dissipative tip–sample forces display peaks at tip–surface distances corresponding to the expulsion of the last two molecular layers. The physical origin of (apparent) superimposed oscillations observed at certain drive frequencies is discussed. analysing the relative strength of various contributions to the cantilever damping. We identify an upper limit for the possible confinement-induced enhancement of the effective viscosity.

2. Materials and methods

2.1. Materials

Amplitude–phase-distance (APD) curves were measured in octamethylcyclotetrasiloxane (OMCTS purum, $\geqslant$99.0%, Sigma Aldrich), a non-polar liquid of slightly spheroid molecules with a major diameter of 1.0–1.1 nm and a minor diameter of 0.7–0.8 nm, which is known to display pronounced layering when confined between two solid surfaces [2–11, 15]. To minimize the detrimental effect of residual water [16] we dried the liquid using 4 Å molecular sieves (Sigma Aldrich) for several days prior to the measurement. To test whether water contamination influenced our results, we repeated the measurements in a closed chamber with a dry nitrogen atmosphere, which gave the same results (within experimental error). As a substrate hydrophobic highly ordered pyrolytic graphite (HOPG, Mikromasch grade ZYA) was used, which was cleaved using adhesive tape just prior to the deposition of the liquid (OMCTS). Before each spectroscopy experiment, the freshly cleaved HOPG substrate was imaged in the liquid to ensure that the surface was clean and atomically smooth and that the system was stable.

2.2. AFM measurements

The measurements were performed on a commercial Veeco Multimode with Nanoscope V controller equipped with a low-noise head using deflection detection and a stable small piezo scanner ('Veeco A scanner'). We used rectangular cantilevers (Mikromasch NSC36, manufactured of bare silicon or gold-coated silicon) with various stiffnesses of $k_c = 3$–7 N m^{-1} and resonance frequencies of $f \approx 80$–120 kHz (in air), as determined using the thermal calibration method [17][1]. The resonance frequency ($f \approx 30$–60 kHz) and quality factor Q ($\sim$3) in liquid were determined with the same method at a reference distance of 100 nm above the sample surface (with a relative uncertainty of $<$5%). The specific cantilevers were chosen for their long tip height ($h \sim 25$ μm) in order to minimize the change in hydrodynamic squeeze-out damping between the cantilever and the solid surface. We verified that possible variations of the added mass and hydrodynamic damping around the cantilever were below the detection limit between the reference distance and 10 nm above the surface. Prior to the measurements the cantilevers were treated in a plasma cleaner (Harrick Plasma) for 1 min. After the measurements the tip was imaged using high resolution SEM (HR-SEM Zeiss LEO 1550) yielding tip radii of $R_{tip} = 15$–30 nm. The cantilever oscillation was driven at the base using a modified tapping holder (Veeco MMMC), as described in [18]. This yields stable drive amplitudes for several hours and reduces the spurious resonance peaks that are typical of commercial liquid cells.

APD curves including the average (tapping mode, TM) deflection signal were recorded over 10 nm tip–surface distances for variable free oscillation amplitudes and drive frequencies from 0.07 to 0.5 nm at large distance (corresponding to peak-to-peak amplitudes of 0.14–1 nm) and 5–60 kHz, respectively. For each setting a minimum of 25 measurement curves were recorded and analysed. The deflection signal in contact with the substrate was used to calibrate the deflection signal, which is appropriate for both static and dynamic deflection since we use small cantilevers compared the size of the laser spot [19] (see also

[1] We used the 'Thermal Tune' in the Nanoscope 7.20 software, which takes all the relevant corrections (e.g. temperature, cantilever shape) into account.

figure 1 supplementary data available at stacks.iop.org/Nano/21/325703/mmedia). Thanks to the small drive amplitudes, no higher harmonics were generated within the (Brownian) noise limit of our system, as verified using a spectrum analyser.

Typically, all APD curves in a set of measurements displayed several oscillations in the amplitude and phase response (see also section 4.1) over a period of several hours. Cantilevers that did not display this stability (e.g. due to a bad tip or contamination) were discarded. Test measurements did not display any significant dependence of the results on the approach speed within a range of 1–10 nm s^{-1}. Therefore a convenient standard approach speed between 1 and 2 nm s^{-1} was chosen for all the experimental data presented here. The drift normal to the surface was typically 0.08 ± 0.03 nm s^{-1}, as determined from the change in z piezo-voltage at tip–surface contact. All measurements were performed at a room temperature of $22 \pm 1\,^{\circ}$C. The temperature next to the sample was measured to be $27\,^{\circ}$C, presumably due to local heating from the electronics in the AFM head.

2.3. Numerical calculations

We simulated the dynamics of the AFM cantilever numerically using the approach of Garcia and Perez [20]. The programs for the simulations were written and run in Matlab based on the code used in [21]. The ordinary differential equation for the cantilever dynamics including the tip–sample forces (see below) was solved using a fourth-order Runge–Kutta scheme. Numerical APD curves for various drive amplitudes were calculated starting 10 nm above the sample surface down to 1 nm in 250 discrete steps. At each step, the steady state amplitude and phase of the oscillation were extracted from the oscillatory cantilever motion via a fast Fourier transform. For fitting and validation purposes, the resulting numerical amplitude and phase versus distance curves were converted into a distance-dependent stiffness using the same force inversion formulae (to be described in section 3) as for the experimental data.

3. Cantilever dynamics and force inversion

Over more than a decade many methods have been developed to quantitatively map both the conservative and dissipative interaction forces in dynamic AFM based on different methods and techniques, varying from small- [14] to large-amplitude [22] AFM as well as universal methods for both amplitude modulation (AM) [23–25] as well as frequency modulation (FM) AFM [26]. In this paper we used AM small-amplitude spectroscopy.

For typical base-driven atomic force microscopes the vertical motion $z(t)$ of the cantilever tip can be modelled as a harmonic oscillator affected by the tip–sample interactions F_{ts}:

$$m\ddot{z} + \gamma_c\dot{z} + k_c z = k_c z_b + F_{ts}. \tag{1}$$

Here, k_c is the cantilever's spring constant, $z_b(t)$ describes the displacement of the cantilever base, m is the total effective mass (including the added mass caused by the motion of the surrounding liquid) and γ_c is the viscous damping around the cantilever. The usual deflection detection scheme measures the deflection $d(t)$ of the cantilever, which is related to the vertical tip position by $z(t) = d(t) + z_b(t)$ (see also figure 1). Since the quality factor Q is low in a liquid environment, both $d(t)$ and $z_b(t)$ can be comparable (see, e.g., [14]). In particular for driving frequencies off resonance the absolute motion of the tip with respect to the sample surface can be significantly larger than the measured deflection amplitude, which has important consequences for the amplitude and phase response of the cantilever (see also [15, 27]).

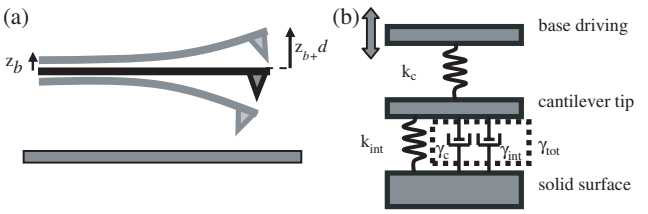

Figure 1. (a) Illustration of the cantilever, where the total motion z of the cantilever consists of the measured deflection d plus the base motion z_b due to the acoustic driving mechanism. (b) Spring–dashpot representation of the harmonic oscillator model for acoustic driving with deflection detection and linearized tip–sample forces.

Since we use for our measurements very small amplitudes (much smaller than the characteristic length scale of the changes in the interactions), we can linearize the tip–sample force F_{ts} around the (quasi-statically moved) average cantilever position z_c. A Taylor expansion of F_{ts} yields

$$F_{ts}(z_c + z, \dot{z}) = F_{ts}(z_c, 0) - k_{int}z - \gamma_{int}\dot{z} - \tfrac{1}{2}k'_{int}z^2 - \gamma'_{int}z\dot{z} + \text{H.O.T.} \tag{2}$$

where H.O.T. are the higher-order terms, $k_{int} = \frac{dF_{ts}}{dz}|_{z_c}$ is the interaction stiffness, γ_{int} is the interaction damping (see figure 1) and $F_{ts}(z_c, 0)$ is the equilibrium force on the cantilever, which shows up in the average deflection. For small static forces and small drive amplitudes, only the linear terms need to be considered, $F_{ts}(z_c + z, \dot{z}) = -k_{int}(z_c)z - \gamma_{int}(z_c)\dot{z}$, leading to a simplified version of equation (1):

$$m\ddot{z} + \gamma_{tot}\dot{z} + k_{tot}z = k_c z_b \tag{3}$$

where $k_{tot} = k_c + k_{int}$ and $\gamma_{tot} = \gamma_c + \gamma_{int}$ are the total stiffness and damping, respectively.

We solve equation (3) using the ansatz $z(t) = A_{tot}\exp(i(\omega t + \varphi_{tot})) = d(t) + z_b(t) = A\exp(i(\omega t + \varphi)) + A_b\exp(i\omega t)$, in which ω is the drive frequency, A and φ are the measured deflection amplitude and phase of the deflection and A_b is the amplitude of the base motion [15]:

$$A = \frac{A_b\sqrt{(k_c - k_{tot} + m\omega^2)^2 + (\omega\gamma_{tot})^2}}{\sqrt{(k_{tot} - m\omega^2)^2 + (\omega\gamma_{tot})^2}} \tag{4a}$$

and

$$\tan\varphi = \frac{-k_c\omega\gamma_{tot}}{k_c(-m\omega^2 + k_{tot}) - (-m\omega^2 + k_{tot})^2 - (\omega\gamma_{tot})^2}. \tag{4b}$$

As noted earlier, the total amplitude A_{tot} of the tip motion, given by $A_{tot} = \sqrt{(A\sin\varphi)^2 + (A\cos\varphi + A_b)^2}$, can be

substantially larger than the measured deflection amplitude A in equation (4*a*).

In order to extract the physical interaction forces we need to solve these expressions for the interaction stiffness k_{int} and damping γ_{int}, yielding

$$k_{\mathrm{int}} = -k_{\mathrm{c}} + m\omega^2 + \frac{k_{\mathrm{c}} A_{\mathrm{b}}(A_{\mathrm{b}} + A\cos\varphi)}{A_{\mathrm{b}}^2 + A^2 + 2A_{\mathrm{b}}A\cos\varphi} \qquad (5a)$$

and

$$\gamma_{\mathrm{int}} = \frac{-k_{\mathrm{c}} A_{\mathrm{b}} A\sin\varphi}{\omega(A_{\mathrm{b}}^2 + A^2 + 2A_{\mathrm{b}}A\cos\varphi)} - \gamma_{\mathrm{c}} \qquad (5b)$$

where A_{b} is calculated from the measured free amplitude A far away from the surface (at 10 nm) using equation (4*a*) with the interactions set to zero[2]. Note that these physical parameters k_{int} and γ_{int} are independent of the specific measurement technique and should look identical as equivalent data extracted from, for example, frequency modulation AFM measurements. Close to resonance, these formulae can be applied using frequency-independent calibration constants (k_{c}, m and γ_{c}) as determined from calibration measurements of the resonance frequency and the Q factor far away from the surface (at 100 nm). For drive frequencies varying over a substantial range, however, one needs to take into account the frequency dependence of the motion of the fluid around the oscillating cantilever [29], which can be achieved by replacing m and γ_{c} by their frequency-dependent counterparts without changing the structure of equations (4) and (5). Following Sader [30], we describe the hydrodynamic loading on the cantilever by a hydrodynamic function $\Gamma = \Gamma' + \mathrm{i}\Gamma''$, which yields an added mass and a damping given by $m_{\mathrm{added}} = \rho\frac{\pi}{4}w^2 L\Gamma'$ and $\gamma_{\mathrm{c}} = \rho\frac{\pi}{4}w^2 L\omega\Gamma''$ [31]. Here, ρ, w and L denote resp. the density of liquid, and the width and the length of the cantilever. Γ depends on the viscous penetration depth $\delta = \sqrt{\frac{2\eta}{\rho\omega}}$ (η: viscosity of the liquid) and the cantilever geometry as $\Gamma' = a_1 + a_2\frac{\delta}{w}$ and $\Gamma'' = b_1\frac{\delta}{w} + b_2(\frac{\delta}{w})^2$ with $a_1 = 1.0533$, $a_2 = 3.7997$, $b_1 = 3.8018$ and $b_2 = 2.736$. Using the calibration constants (k_{c}, Q_{air}, Q_{liq}, $\omega_{\mathrm{res,air}}$ and $\omega_{\mathrm{res,OMCTS}}$) applied at resonance allows for calculating the frequency-independent prefactor in both the frequency-dependent added mass and damping.

The relevance of this frequency-dependent correction becomes apparent from the amplitude and phase response of the cantilever far away from the surface. Figure 2 shows a comparison between the experimental frequency response (thick black solid lines) and various implementations of the model. Above the resonance frequency, the experimental data are distorted by various spikes, which are typical for AFMs with acoustic driving. To avoid interference with these features, all measurements described in this paper are carried out at drive frequencies below the lowest spike. We therefore also limit the comparison of the model curves to the frequency range below resonance. The blue dashed lines show the response curve of a simple harmonic oscillator (ignoring the base motion), which is shown for reference and which is obviously not suitable in the present case of a low Q environment [14, 15, 27]. The red thin solid curves represent the frequency response according to equations (4) (i.e. including the base motion) for constant m and γ_{c}. As described in [15], this correction captures the most important features of the experimental curves, namely the vanishing amplitude and the non-zero phase at low frequencies. Yet, the phase decreases much more quickly towards $-90°$ than observed experimentally, which was left unnoticed previously. This deviation leads to a substantial phase error if the model is used to extract tip–sample interaction forces from measured APD curves at low frequencies. In contrast, the green dashed–dotted model curve, which incorporates the frequency dependence of m and γ_{c}, produces a much more satisfying agreement also at the lowest frequencies and thus reproduces the global shape of both amplitude and phase response over the entire frequency range—notwithstanding some residual deviations.

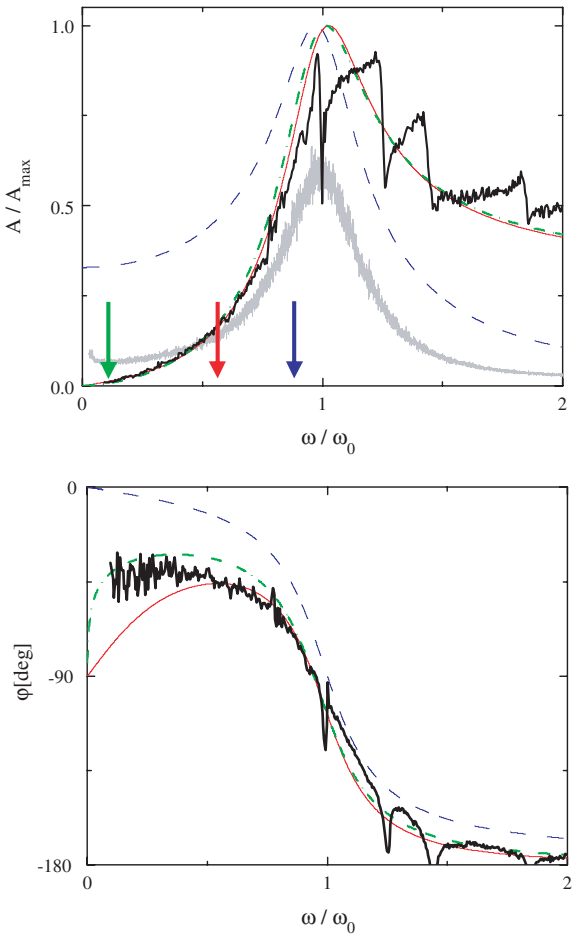

Figure 2. Amplitude and phase response of the cantilever versus normalized drive frequency for ambient liquid ($Q = 3$). Blue dashed lines: conventional harmonic oscillator (H.O.). Red solid lines: deflection signal including base drive (constant damping and added mass). Green dashed–dotted lines: deflection signal including base drive with frequency-dependent damping and added mass. Black lines: experimental response (Au-coated Si cantilever, $\omega_{\mathrm{res}}/2\pi = 38$ kHz, the spurious peaks above $\omega/\omega_0 = 0.95$ are due to the piezo response). Grey line: thermal noise spectrum (Si cantilever, $\omega_{\mathrm{res}}/2\pi = 42$ kHz). Coloured arrows indicate the measurement frequencies of the data shown in figure 3.

[2] Somewhat differently looking, but equivalent, force inversion formulae were derived by Jai *et al* [28].

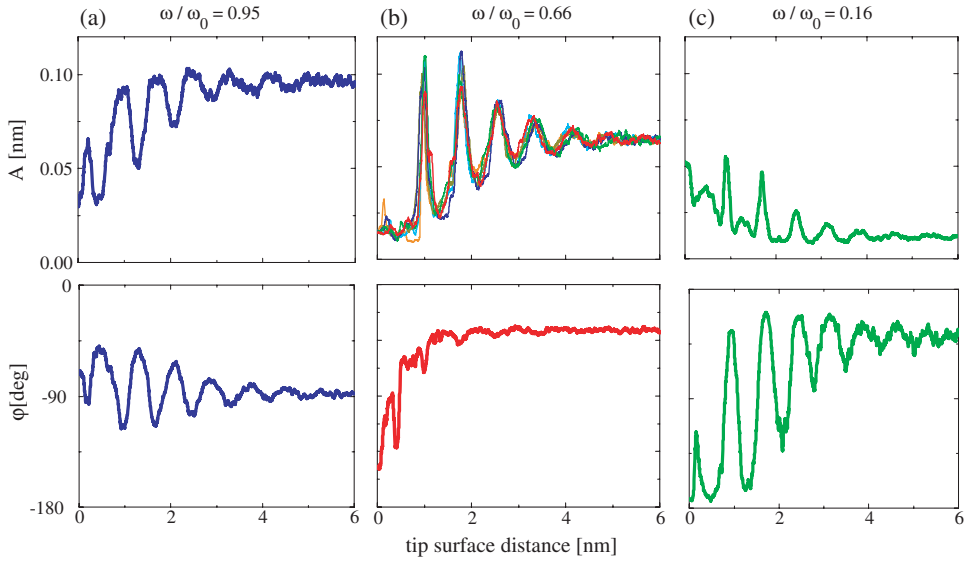

Figure 3. Amplitude A and phase φ versus distance curves upon approaching the surface (total free amplitude (a) 0.117 nm, (b) 0.129 nm and (c) 0.320 nm; resonance frequency $\omega_{\rm res}/2\pi = 38$ kHz, Au-coated Si cantilever) for three different driving frequencies: (a) $\omega/\omega_0 = 0.95$, (b) $\omega/\omega_0 = 0.66$ and (c) $\omega/\omega_0 = 0.16$. The different curves in (b) indicate the reproducibility of the measurements (a smoothing filter was applied to eliminate high frequency noise).

4. Results

4.1. Measurements

Figure 3 shows APD curves measured with the same cantilever at three different frequencies close to and below resonance. We chose these frequencies with special care. At these frequencies the calculated cantilever response matches the measured response very well and no spurious peaks were observed in the spectra (figure 2). For all driving frequencies, both the amplitude and the phase display oscillations with a periodicity varying from 0.7 to 0.9 nm from curve to curve reflecting the diameter of the OMCTS molecules. Close to resonance (figure 3(a), $\omega/\omega_0 = 0.95$), the oscillations are clearly visible in both the amplitude and the phase signal. The oscillations in the phase are approximately symmetric around $-90°$. The oscillations in the amplitude are superimposed on an overall decrease of the amplitude at small distances. On the wing of the resonance peak (figure 3(b), $\omega/\omega_0 = 0.66$), the oscillations in the amplitude are stronger and more peaked (the different curves indicate the reproducibility), while they almost disappear in the phase response. At the lowest frequency (figure 3(c), $\omega/\omega_0 = 0.16$), a strongly oscillatory response appears again in the phase, whereas the oscillations in the amplitude become less pronounced and are superimposed on an overall increase towards small distances. The same trends as a function of frequency are observed for all free amplitudes. For the highest free amplitudes, the amplitude and phase modulations decrease systematically, as noted earlier by others [8]. Using the results of figure 2 we can qualitatively understand the frequency-dependent response in figure 3, as already discussed in [15]. Briefly, at resonance ($\omega/\omega_0 = 0.95$) the slope in the amplitude response is smaller than on the wing ($\omega/\omega_0 = 0.66$), leading to a less-pronounced amplitude response in figure 3(a) than in figure 3(b), whereas the opposite holds for the phase response. The strong phase response at low frequencies is caused by the base driving scheme. As discussed in [15], the phase response (red thin solid lines) shows a gradual reduction in the phase to $-90°$ for $\omega \to 0$. In this limit, equation (4*b*) can be approximated by $\tan\varphi_{\omega\to 0} \approx \frac{\omega\gamma_t}{k_{\rm int}(1+k_{\rm int}/k_{\rm c})}$, which is very sensitive to changes in the interaction stiffness $k_{\rm int}$. In particular, φ is expected to vary between zero and 180° for $\omega \to 0$ as $k_{\rm int}$ changes sign as a function of distance, as is the case for oscillatory solvation forces.

The data in figure 3 represent typical APD curves selected from a large dataset. The overall behaviour of the curves is very reproducible, as evidenced by the selection of amplitude curves shown in figure 3(b). Yet, details such as the number of visible oscillations cycles can vary from curve to curve. Figure 4 shows the distribution of the number of oscillations observed in a number of consecutive APD curves at several locations on the sample surface under otherwise identical conditions. Regarding the fact that the tip–sample interaction is mediated by merely a few hundred molecules under the tip, we attribute the variations in the number of oscillations to the stochastic nature of the molecular motion. This distribution does not affect the validity of the qualitative trends as a function of frequency shown in figure 3.

4.2. Analysis of the measurements

4.2.1. Tip–sample interaction forces. To extract the tip–sample interaction forces from the measured data, we apply equations (5) to the measured APD curves shown in figure 3. Before doing so, we need to realize that the measured phase is affected by a phase offset due to the measurement system. The agreement between the experimental phase response and the model curve in figure 2 shows that (except for the spurious peaks at high frequencies) this phase offset is a frequency-independent constant. To account for it, we measure the

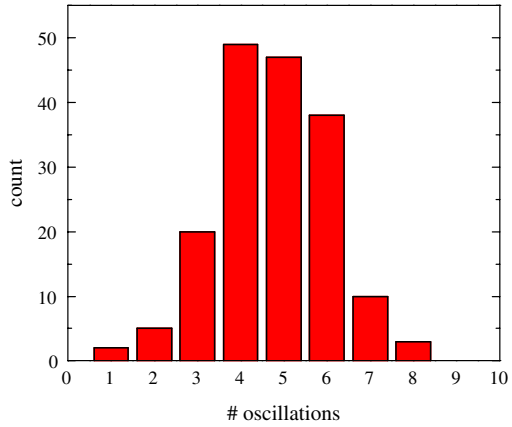

Figure 4. Frequency of the number of oscillations in amplitude–distance curves from 174 measurements at six different positions on different terraces of the HOPG ($\omega/\omega_0 = 0.75$).

phase at a distance of 10 nm above the surface (i.e. outside the range of the tip–sample interaction) and shift this value manually to the value obtained from the model curve following a procedure suggested by Sader and Jarvis [32] in the context of frequency modulation AFM measurements. Failure to carry out this procedure correctly leads to cross-coupling between the phase and amplitude signal and thereby induces two main effects: (i) the interaction stiffness and the interaction damping do not decay to zero at large distance and (ii) artificial oscillations in the dissipation are created in the case of oscillatory conservative tip–sample forces (see [8, 13]).

Figure 5 shows the interaction stiffness and damping extracted by inverting the curves shown in figure 3 using equations (5) using the full frequency-dependent m and γ_c. The conservative forces display a strongly oscillatory behaviour that decays to zero within a few molecular layers, independent of the applied frequency. The only significant trend (i.e. beyond typical variations from curve to curve) is a slight reduction of the amplitude of the force oscillations at the lowest frequencies. Yet, as we will discuss below, this effect is caused by the somewhat larger drive amplitude required in off-resonance measurements.

The extracted total damping shows more variability between the different drive frequencies. For $\omega/\omega_0 = 0.95$ and 0.66, an oscillatory behaviour appears, similar to and exactly out-of-phase with the interaction stiffness with superimposed peaks. For the lowest drive frequency, the oscillatory behaviour is absent, yet the peaks at $d \approx 0.9$ and 1.7 nm remain visible. Such sharp peaks in the total damping were consistently found in many independent experiments with various cantilevers (Si or gold-coated Si and for various tip radii and spring constants). Note that the total damping at large distance approaches a constant value $\gamma_{\mathrm{tot}}^{\infty}$, which decreases with decreasing frequency as expected from the expressions given in section 3.

The degree of consistency shown in figure 5 can only be achieved using the complete mechanical model for acoustic driving with deflection detection (see figure 1) including the frequency-dependent damping and added mass presented in section 4.1. Neglecting the frequency dependence of the added mass and damping leads to substantial deviations of the damping forces at low frequencies. If the base motion is neglected (i.e. upon using a simple harmonic oscillator model) both conservative and dissipative forces are completely inconsistent between low and high frequencies, as expected (see [14]). Both of these findings are obviously consistent with the deviations found for the modelled frequency response curves (figure 2).

4.2.2. Conservative forces and amplitude dependence. For tip–surface distances beyond 1 nm, the conservative force curves can be fitted rather well with an exponentially decaying cosine profile (see figure 2, supplementary data available at

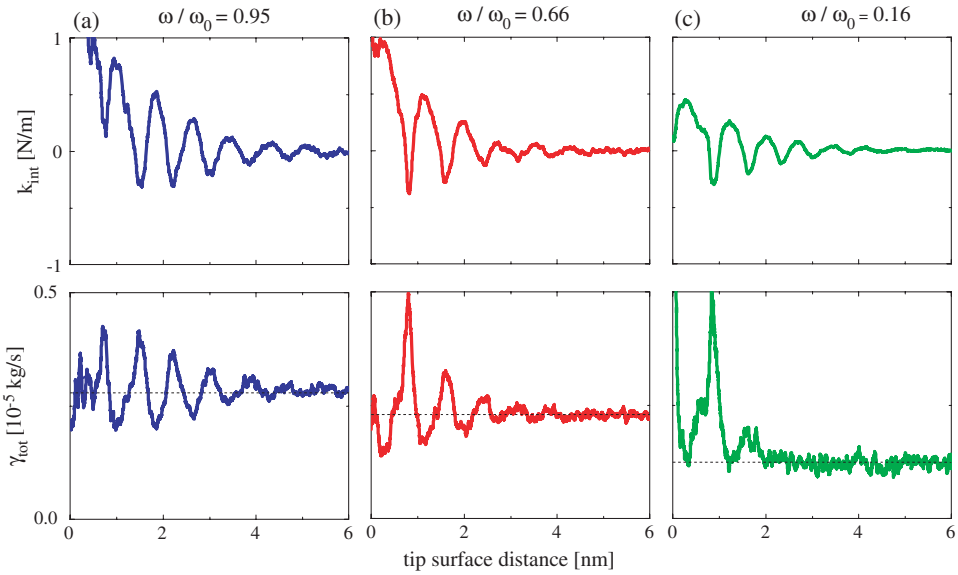

Figure 5. The interaction stiffness k_{int} and total damping γ_{tot} versus tip–surface distance extracted from the amplitude and phase response of the cantilever (curves in figure 3) using equations (5) with frequency-dependent damping and added mass. Left column: $\omega/\omega_0 = 0.95$; middle: $\omega/\omega_0 = 0.66$; right: $\omega/\omega_0 = 0.16$. The black dashed lines denote the damping of the cantilever γ_c.

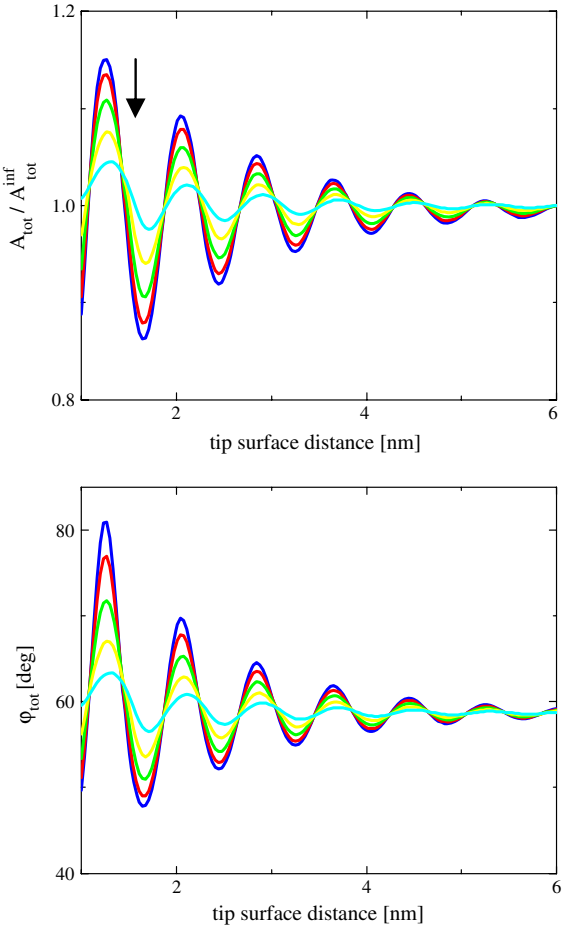

Figure 6. Numerically calculated amplitude and phase response of the cantilever ($\omega/\omega_0 = 0.93$, $k_c = 1.9$ N m^{-1} and $Q = 2.7$) versus tip–surface distance in the presence of oscillatory tip–sample forces ($K_{int} = 0.3$ N m^{-1}, $\sigma = 0.8$ nm and $\xi = 1.1$ nm) for variable free amplitude (80 pm, 160 pm, ... 400 pm) increasing along the arrow from dark blue to turquoise.

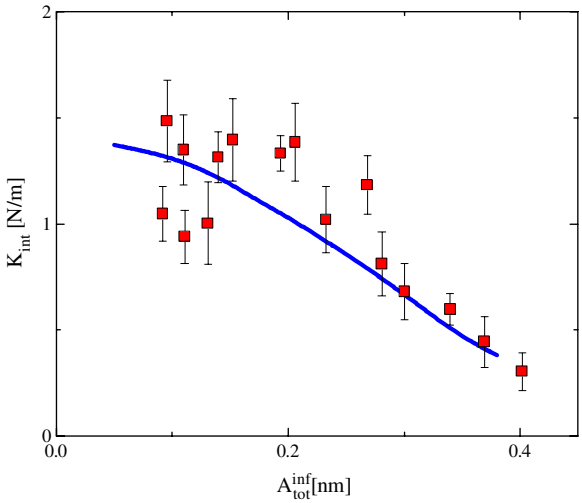

Figure 7. Apparent amplitude K_{int} of the fitted interaction stiffness versus total cantilever amplitude A^{∞}_{tot} extracted from the amplitude and phase response ($\omega/\omega_0 = 0.92$, resonance frequency $\omega_0/2\pi = 36$ kHz). Symbols: experimental results (Si cantilever); error bars denote the standard error with 95% confidence interval. Solid line: numerical calculation (see text for details).

stacks.iop.org/Nano/21/325703/mmedia), which is known to approximate the shape of oscillatory solvation forces rather well [2]:

$$k_{int}(z_c) = K_{int}\cos(2\pi z_c/\sigma)\exp(-z_c/\xi). \qquad (6)$$

Fitting equation (6) to the experimental data at variable frequency, we find an average periodicity $\sigma = 0.78 \pm 0.1$ nm and a decay length $\xi = 1.2 \pm 0.2$ nm. Equation (6) provides a good fit to the experimental data for distances beyond the first molecular layer, as illustrated in supplementary data (figure 2 available at stacks.iop.org/Nano/21/325703/mmedia). (The region $d <\sim 0.75$ nm was excluded in the fitting process.) The fitting parameter K_{int} yields a measure for the strength of the oscillatory solvation forces.

Before comparing the data at variable frequencies, we note that the (apparent) strength of the oscillatory solvation forces depends on the amplitude of the cantilever oscillation. If the free amplitude of the cantilever becomes comparable to the characteristic length scale of the interactions the amplitude of the oscillations in both amplitude and phase as well as in the resulting interaction forces decreases, as shown in figure 6 (see also [8]). Converting APD curves obtained for variable A^{∞}_{tot} between 0.09 and 0.4 nm at a fixed frequency into interaction forces and fitting the conservative forces using equation (6), we find experimentally that the amplitude of the interaction stiffness gradually decreases approximately from 1.2 N m^{-1} for the smallest amplitude to 0.3 N m^{-1} for the largest amplitude (see symbols in figure 7)[3].

In the context of the force inversion method used here, the linearization of the tip–sample interaction forces, as described in equation (2), provides a criterion for the maximum acceptable total amplitude A^{∞}_{tot}. For typical numbers for the periodicity $\sigma = 0.8$ nm and for the decay length $\xi = 1.1$ nm, we find the requirement $A^{\infty}_{tot} \ll 2k_{int}/k'_{int}$, so $A^{\infty}_{tot} \ll 0.29$ nm. To quantify the expected reduction, we calculated APD curves inserting the full nonlinear tip–sample interaction force according to equation (6) into (1) for variable driving amplitude at a fixed drive frequency close to resonance. (For simplicity the interaction damping was left out in these calculations.)

As shown in figure 6, the amplitude of the oscillations in A_{tot} and φ_{tot} decreases strongly with increasing A^{∞}_{tot}, in qualitative agreement with the experimental data. Note that appreciable smoothing effects can already be observed for $A^{\infty}_{tot} = 0.16$ nm.

Inserting the numerically calculated cantilever response into equations (5) leads to the apparent interaction stiffness as a function of the free cantilever amplitude. The solid line in figure 7 shows the corresponding stiffness amplitude K_{int} decreases as a function of A^{∞}_{tot}, in excellent agreement with experimental measurements.

[3] To exclude the possibility of systematic changes in the experimental conditions with time, e.g. due to contamination or temperature variation, the free amplitude was increased and decreased in random order during the experiments.

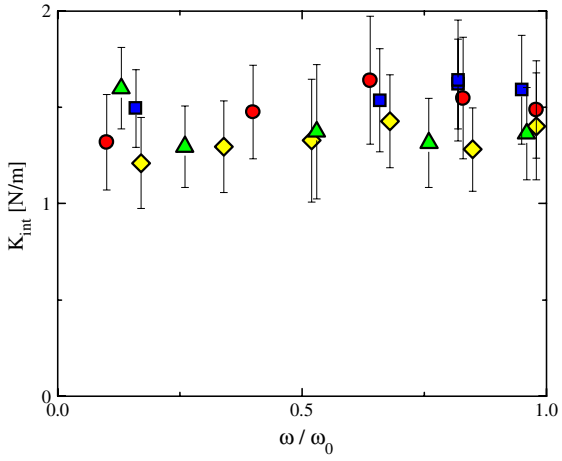

Figure 8. Extrapolated amplitude $K_{\rm int}$ of the fitted interaction stiffness versus measurement frequency for various cantilevers. (Red circles: Au-coated Si, $\omega_{\rm res}/2\pi = 51$ kHz; green triangles: Si, $\omega_{\rm res}/2\pi = 37$ kHz; yellow diamonds: Si, $\omega_{\rm res}/2\pi = 59$ kHz; blue squares: Au-coated Si, $\omega_{\rm res}/2\pi = 38$ kHz; error bars denote the standard error with 95% confidence interval.)

This result explains the apparent reduction of the oscillatory interaction forces in figure 5(c) (recorded far below resonance) compared to figures 5(a) and (b) (recorded on resonance): the off-resonance measurements were performed using a relatively large amplitude $A_{\rm tot}^{\infty} \approx 0.3$ nm (see figure 3) in order to achieve a similar signal-to-noise ratio as for the on-resonance measurements. For such large amplitudes, linearization of the tip–sample interaction forces is no longer justified, causing the observed apparent reduction of $K_{\rm int}$.

This observation may explain some of the discrepancies between different dynamic AFM measurements carried out with different free amplitudes.

4.2.3. Conservative tip–sample interaction at variable drive frequency. Using the result of figure 7, we can correct the extracted apparent values of the amplitude of the interaction stiffness $K_{\rm int}$ and extrapolate them to their intrinsic value for small drive amplitudes. Figure 8 shows the result for a dataset consisting of various different cantilevers and types of cantilevers for a range of drive frequencies from 5 to 58 kHz. Within the experimental error, we find that the strength of the oscillatory solvation forces is identical, irrespective of the drive frequency and of the material of the cantilever.

5. Discussion

5.1. Conservative tip–sample interaction

To compare the present results to previous SFA and AFM measurements, we convert the interaction stiffness $k_{\rm int}$ into the normalized force f/R using the Derjaguin approximation [19, 33, 34]. f/R is proportional to the interaction energy per unit area of two parallel surfaces at separation $z_{\rm c}$. Approximating the local oscillatory pressure by $P(z_{\rm c}) = P_0 \cos(2\pi z_{\rm c}/\sigma)\exp(-z_{\rm c}/\xi)$, the resulting *amplitude* F/R of the distance-dependent oscillatory force f/R is related to the *amplitude* $K_{\rm int}$ of the distance-dependent oscillatory stiffness $k_{\rm int}$ (fitted using equation (6)) by

$$\frac{F}{R} = \frac{K_{\rm int}}{2\pi R\sqrt{(\frac{1}{2\pi\xi})^2 + (\frac{1}{\sigma})^2}} \tag{7}$$

where R is the tip radius. For small drive amplitudes and using the fitted interaction stiffness, we find a force amplitude $F/R = 9 \pm 2$ mN m^{-1}, in agreement with earlier measurements in SFA and AFM [2, 33]. Based on the fact that tip–sample distances of about one molecular layer and below need to be excluded from the fitting procedure, one may speculate that the molecules immediately adjacent to the substrate surface are in a different, perhaps solidified, state as compared to the other molecular layers.

The fact that the strength of the solvation forces extracted from distances beyond the first molecular layer is independent of the drive frequency indicates that the system does not have any relevant relaxation times within the corresponding time interval of 0.02–0.2 ms. For a fluid this is not surprising since typical molecular relaxation times are substantially faster.

5.2. Dissipative tip–sample interaction

Compared to the conservative interactions, the picture emerging from the dissipation extracted for various frequencies is somewhat less consistent. For all frequencies the dissipation decays to a constant frequency-dependent asymptotic value $\gamma_{\rm tot}^{\infty}(\omega)$, as expected. Yet, the data recorded close to resonance (figures 5(a) and (b)) display oscillations involving both enhancements and reductions of $\gamma_{\rm tot}$ by several tens of per cent of $\gamma_{\rm tot}^{\infty}$, while the low frequency data (figure 5(c)) only display positive peaks at distances corresponding to the minima in $k_{\rm int}$.

To elucidate whether oscillations in the damping are realistic and to what extent confinement may enhance the local dissipation, we consider the dynamics of the cantilever in the framework of hydrodynamics. The experimental observation that A and φ (as well as $k_{\rm int}$ and $\gamma_{\rm tot}$) are constant within several tens of nanometres from the surface (see section 2 and figure 3 of supplementary data available at stacks.iop.org/Nano/21/325703/mmedia) suggests that it is justified to split the dissipation into a background contribution due to the global motion of the cantilever, which is constant within the distance range covered by the APD curves, and a distance-dependent contribution arising from the local dynamics in the vicinity of the tip. This idea is consistent with an approach by O'Shea and Welland [11], who decomposed the total damping into separate contributions arising from the motion of different parts of the cantilever, namely the cantilever beam, the cone of the tip (modelled as an effective sphere) and the nanoscale tip itself. For each of these components separate solutions of the time-dependent Stokes equations for the respective idealized geometry are known and allow for estimating their relative importance. The analysis, which we describe for our experimental situation in the appendix, shows that the total damping is dominated by the damping of the cantilever beam in the fluid rather than the squeeze-out damping at the tip. This is due to the much larger characteristic size of the former

(typically 100 μm versus 20 nm). Inserting numerical values, one finds indeed that this background contribution is expected to be constant, within ~0.25%, over the range of the APD curves. The most interesting distance-dependent contribution is obviously the squeeze-out damping due to the confined fluid the between tip and sample. It can be described by Reynolds' classical expression:

$$\gamma_R = 6\pi\,\eta_{loc}\frac{R_{tip}^2}{d}. \tag{8}$$

For distances d of a few nanometres and for a local viscosity η_{loc} under the tip equal to the bulk viscosity, this tip damping is several orders smaller than the beam damping [11]. Only for $d \to 0$ (i.e. $\ll$1 nm) and/or if the local viscosity is dramatically enhanced, e.g. due to confinement effects, this contribution can lead to a substantial and measurable excess damping.

The above considerations have important consequences regarding the nature of variations in the damping, which—to our knowledge—have not been expressed explicitly so far: since the background damping is constant within the experimental error and a few orders of magnitude larger than the tip damping, γ_{tot} can only increase but never significantly decrease within the uncertainty of AFM measurements (typically a few per cent). This conclusion results directly from the relative order of magnitude of the global and the local dissipation and therefore applies to all AFM measurements independent of the specific measurement technique (AM-AFM versus FM-AFM; base drive versus magnetic drive). As a consequence, we conclude that any reduction of the global damping, such as the ones shown in figures 5(a) and (b), must be artificial and caused by either uncertainties in calibration constants and/or imperfections in the model of the cantilever dynamics. (For the present case of AM-AFM, the experimental uncertainties include in particular errors in the absolute phase [8, 13], in addition to Q and ω_0, which are also important in FM-AFM.)

Since the background damping of the cantilever is constant within the experimental errors, it is justified to subtract that contribution and consider the remaining interaction damping $\gamma_{int} = \gamma_{tot} - \gamma_{tot}^{\infty}$. Using hydrodynamics as a reference framework, we compare the resulting γ_{int} to the expectations based on equation (8) (see figure 9).

We plot the low frequency data from figure 5(c) in figure 9 because they do not display artificial negative values of γ_{int}, caused by excessive reductions of γ_{tot} as discussed above. Moreover, the low frequency measurements are less sensitive to calibration errors, while the amplitude and phase response (as mentioned above) is equally sensitive to variations in the stiffness and damping (see also supplementary data available at stacks.iop.org/Nano/21/325703/mmedia and partially [15]).

Figure 9 also shows the calculated Reynolds squeeze-out damping under the tip (equation (8)), for increasing values of the viscosity. For $\eta_{loc} = \eta_{bulk}$ (figure 9), the Reynolds damping under the tip γ_R is negligible for all realistic values of d, in agreement with the discussion above. Yet, the Reynolds damping resulting from an already 100 times enhanced local viscosity lies above the experimental data at all distances.

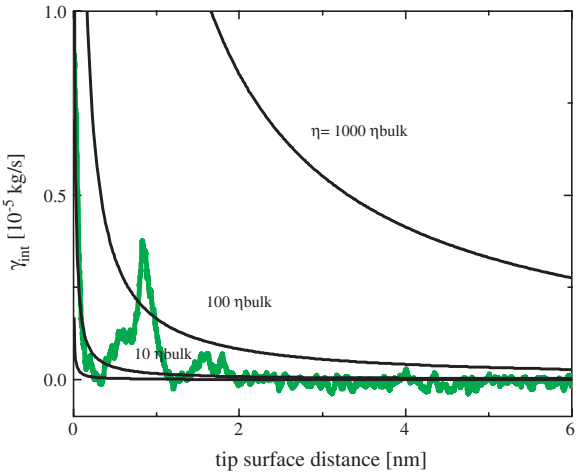

Figure 9. The extracted interaction damping for $\omega/\omega_0 = 0.16$ (green curve). The black curves show the calculated Reynolds damping γ_R for increasing viscosity ($R_{tip} = 20$ nm).

In the damping measured for $d > 2$ nm, the data are consistent with the bulk viscosity and approximately 10$\times$ the bulk viscosity (within the experimental error), corresponding to 22 mPa s. Larger enhancement factors are incompatible with our experimental data. Note that the same conclusion can also be drawn on the basis of all our data recorded, irrespective of the drive frequency (including the artificial oscillations visible close to resonance).

A direct conversion of the measured damping into an effective viscosity seems to provide a reasonable description of the system down to distances of 2–3 nm. At smaller separations, the hydrodynamic picture becomes progressively more questionable given the small number of molecules involved (a few hundred) and the discrete layer structure of the confined liquid. The position of the maxima at $d \approx 0.9$ and 1.7 nm in the damping in figure 9 coincides with the minima in the interaction stiffness. It also coincides with a region of (small) negative slope of the average deflection of the cantilever (data not shown). The maxima in the damping thus occur at distances corresponding to attractive forces, where according to a standard hard sphere-like model as well as numerical simulations, the average density of the fluid inside the gap is reduced compared to the bulk value. Such a reduced density implies more free volume for the molecules and thus more freedom to exchange sites, which may enhance the opportunities to dissipate energy compared to the more compact configuration of completely filled layers that provide a more elastic response. Hofbauer *et al* [12] recently proposed a similar mechanism to explain similar (yet more pronounced) peaks in the dissipation for confined dodecanol.

Finally, we note that for all distances, except for the minima in the interaction stiffness (corresponding to the attractive part of the conservative forces), the damping always assumes values that are compatible with the bulk viscosity, indicating that the 'effective viscosity' in complete layers of OMCTS is similar to the value found in the bulk. Notwithstanding the differences in the confinement geometry between the surface force apparatus and the AFM, it is

remarkable how this result agrees with some of the earlier SFA measurements [5, 6].

The fact that the conservative tip–sample interaction forces follow the behaviour of hard sphere fluids (equation (6)) and the fact that the effective viscosity is compatible with the bulk viscosity down to a thickness of three monolayers clearly suggest that the system behaves liquid-like. The consistency of this behaviour (including in particular the absence of artificial negative interaction damping) for the various experimental conditions investigated support this conclusion. We note that this finding is at variance with the conclusion of Patil *et al* [9] who reported signs of a jamming-like solidification for confined OMCTS for the range of approach rates used in the present study and liquid-like behaviour only for approach rates below 0.6 nm s^{-1}. Their interpretation is based on a Maxwellian model of a viscoelastic liquid, yet they do not provide any details regarding the modelling of the cantilever dynamics. We currently have no explanation for the deviation from our data.

6. Conclusions

In summary, the results presented in this paper show that it is indeed possible to extract consistent tip–sample interaction forces over a wide range of driving frequencies from acoustic drive amplitude modulation AFM measurements provided that three elements are correctly taken into account, namely (i) the motion of the cantilever base, (ii) the frequency dependence of the added mass and the viscous damping around the cantilever and (iii) the finite oscillation amplitude of the cantilever. While the consistency with respect to the conservative forces is very satisfying, known residual discrepancies due to cross-coupling with conservative forces limit the accuracy of dissipative forces measured at AFM drive frequencies close to resonance. This problem can be circumvented by choosing drive frequencies substantially below resonance, where the measurement system is less sensitive to errors in the phase and/or uncertainties in the calibration constants.

The dissipative forces extracted in this way show that the 'effective' viscosity of the liquid confined between tip and sample is bulk-like down to approximately three molecular layers. Only for the last two layers are local maxima in the dissipation found at tip–sample distances corresponding to minima in the interaction stiffness where the average density of the confined fluid is expected to be minimal from molecular simulations.

Acknowledgments

We thank J E Sader for his comments at SPM-UK 2009. We thank P Markus (Veeco) and K Smit for the technical support and M Smithers for his help on the SEM images. This work has been supported by the Foundation for Fundamental research on Matter (FOM), which is financially supported by the Netherlands Organization for Scientific Research (NWO).

Appendix

Consider an AFM cantilever [11] consisting of a rectangular beam with length $L = 120\ \mu$m, width $w = 35\ \mu$m and at the end a tip with cone radius $R_{\rm cone} = 5\ \mu$m and a tip end with radius $R_{\rm tip} = 10$ nm. The cantilever is in the vicinity of a solid surface and completely immersed in a liquid with density $\rho = 2330$ kg m^{-3} and viscosity $\eta = 2.2$ mPa s. The distance between the beam and the surface is $h = d + 25\ \mu$m, between the tip cone and the surface is $D = d + 8\ \mu$m, with the distance between the tip and the surface d (∼1–2 nm).

For each part of the cantilever, there are contributions due to the free oscillation far away from the surface and contributions due to squeeze-out damping close to the surface. The former contain a constant and a frequency-dependent component due to the varying added mass, which is responsible for the reduction of the total damping for large distances at low frequencies (see figure 5).

The total damping of the cantilever is built up by:

(1) Hydrodynamic damping due to viscous drag and the added mass over the beam:

$$\gamma_{\rm cb} = 0.24 \cdot \left(3\pi\eta L + \tfrac{3}{4} w L \sqrt{2\rho\eta\omega}\right).$$

(2) Hydrodynamic damping due to viscous drag and the added mass at the tip cone:

$$\gamma_{\rm cc} = \tfrac{1}{2}(6\pi\eta R_{\rm cone} + 3\pi R_{\rm cone}^2 \sqrt{2\rho\eta\omega}).$$

(3) Hydrodynamic damping due to viscous drag and the added mass at the tip:

$$\gamma_{\rm ct} = \tfrac{1}{2}(6\pi\eta R_{\rm tip} + 3\pi R_{\rm tip}^2 \sqrt{2\rho\eta\omega}).$$

(4) Reynolds squeeze-out damping under the beam, $\gamma_{\rm Rb} = 0.24\eta\frac{w^3 L}{h^3}$.

(5) Reynolds squeeze-out damping under the cone, $\gamma_{\rm Rc} = 6\pi\eta\frac{R_{\rm cone}^2}{D}$.

(6) The interaction damping under the tip, $\gamma_{\rm int}$.

   (a) Reynolds squeeze-out damping under the tip, $\gamma_{\rm int\ R} = 6\pi\eta_{\rm local}\frac{R_{\rm tip}^2}{d}$.

   (b) Changes in the hydrodynamic damping due to local changes in the added mass and viscosity under the tip, $\gamma_{\rm int\ c} = \frac{1}{2}(6\pi(\eta_{\rm local} - \eta)R_{\rm tip} + 3\pi R_{\rm tip}^2(\sqrt{2\rho\eta_{\rm local}\omega} - \sqrt{2\rho\eta\omega}))$.

We define damping 1–5 as the background damping $\gamma_{\rm c}$ and damping 6 as the interaction damping, $\gamma_{\rm int}$.

First of all, using these equations, it is easy to show that, due to the change in Reynolds damping between 100 and 1 nm tip–surface distance, the cantilever's damping $\gamma_{\rm c}$ increases by 0.25%. This is far within our experimental error and therefore our assumption that the extracted changes in damping are due to tip–sample interactions is valid. (Remember that the assumption of a constant $\gamma_{\rm c}$ is supported by the experimental observation that the APD curves are constant for tip–sample distances varying between 100 and 10 nm.)

Second, note that the damping due to the Reynolds force under the tip always results in an increase of the total damping and therefore a positive interaction damping. Consequently the negative interaction damping can only be a result of a change in hydrodynamic damping due to viscous drag and the added mass at the tip. Since the local density (and accordingly the viscosity) under the tip varies around its bulk value, this contribution can be both positive and negative. However, if, in a worst case scenario, the local viscosity under the tip would go to zero, the maximum decrease in the calculated total damping is 0.013%. Our experimentally found decrease in the total damping is much larger and therefore unrealistic.

References

[1] Bhushan B, Israelachvili J N and Landman U 1995 Nanotribology: friction, wear and lubrication at the atomic scale *Nature* **374** 607

[2] Israelachvili J N 1992 *Intermolecular and Surface Forces* 2nd edn (London: Academic)

[3] Klein J and Kumacheva E 1995 Confinement-induced phase transitions in simple liquids *Science* **269** 816

[4] Gee M L, McGuiggan P M, Israelachvili J N and Homola A M 1990 Liquid to solid-like transitions of molecularly thin films under shear *J. Chem. Phys.* **93** 1895

[5] Becker T and Mugele F 2003 Nanofluidics: viscous dissipation in layered liquid films *Phys. Rev. Lett.* **91** 166104

[6] Bureau L and Arvengas A 2008 Drainage of a nanoconfined simple fluid: rate effects on squeeze-out dynamics *Phys. Rev.* E **78** 061501

[7] Gao J, Luedtke W D and Landman U 1997 Layering transitions and dynamics of confined liquid films *Phys. Rev. Lett.* **79** 705

[8] Maali A, Cohen-Bouhacina T, Couturier G and Aimé J-P 2006 Oscillatory dissipation of a simple confined liquid *Phys. Rev. Lett.* **96** 086105

[9] Patil S, Matei G, Oral A and Hoffmann P M 2006 Solid or liquid? solidification of a nanoconfined liquid under nonequilibrium conditions *Langmuir* **22** 6485

[10] Kaggwa G B, Kilpatrick J I, Sader J E and Jarvis S P 2008 Artifact-free dynamic atomic force microscopy reveals monotonic dissipation for a simple confined liquid *Appl. Phys. Lett.* **93** 011909

[11] O'Shea S J and Welland M E 1998 Atomic force microscopy at solid–liquid interfaces *Langmuir* **14** 4186

[12] Hofbauer W, Ho R J, Hairulnizam R, Gosvami N N and O'Shea S J 2009 Crystalline structure and squeeze-out dissipation of liquid solvation layers observed by small-amplitude dynamic AFM *Phys. Rev.* B **80** 134104

[13] O'Shea S J 2006 Comment on 'oscillatory dissipation of a simple confined liquid' *Phys. Rev. Lett.* **97** 179601

[14] Burnham N A, Gremaud G, Kulik A J, Gallo P-J and Oulevey F 1996 Materials' properties measurements: choosing the optimal scanning probe microscope configuration *J. Vac. Sci. Technol.* **14** 1308

[15] de Beer S, van den Ende D and Mugele F 2008 Atomic force microscopy cantilever dynamics in liquid in the presence of tip sample interaction *Appl. Phys. Lett.* **93** 253106

[16] Christenson H K and Blom C E 1987 Solvation forces and phase separation of water in a thin film of nonpolar liquid between mica surfaces *J. Chem. Phys.* **86** 419

[17] Hutter J L and Bechhoefer J 1993 Calibration of atomic force microscopy tips *Rev. Sci. Instrum.* **64** 1868

[18] Maali A, Hurth C and Cohen-Bouhacina T 2006 Improved acoustic excitation of atomic force microscope cantilevers in liquids *Appl. Phys. Lett.* **88** 163504

[19] Proksch R, Schaeffer T E, Cleveland J P, Calahan R C and Viani M B 2004 Finite optical spot size and position corrections in thermal spring constant calibration *Nanotechnology* **15** 1344

[20] Garcia R and Perez R 2002 Dynamic atomic force microscopy methods *Surf. Sci. Rep.* **47** 197–301

[21] Zitzler L, Herminghaus S and Mugele F 2002 Capillary forces in tapping mode atomic force microscopy *Phys. Rev.* B **66** 155436

[22] Hoelscher H 2006 Quantitative measurement of tip–sample interactions in amplitude modulation atomic force microscopy *Appl. Phys. Lett.* **89** 123109

[23] Lee M H and Jhe W H 2006 General theory of amplitude-modulation atomic force microscopy *Phys. Rev. Lett.* **97** 036104

[24] Hu S Q and Raman A 2008 Inverting amplitude and phase to reconstruct tip–sample interaction forces in tapping mode atomic force microscopy *Nanotechnology* **19** 375704

[25] Katan A J, van Es M H and Oosterkamp T H 2009 Quantitative force versus distance measurements in amplitude modulation AFM: a novel force inversion technique *Nanotechnology* **20** 165703

[26] Sader J E and Jarvis S P 2004 Accurate formulas for interaction force and energy in frequency modulation force spectroscopy *Appl. Phys. Lett.* **84** 1801

[27] Xu X and Raman A 2007 Accurate force spectroscopy in tapping mode atomic force microscopy in liquids *J. Appl. Phys.* **102** 034303

[28] Jai C, Cohen-Bouhacina T and Maali A 2007 Analytical description of the motion of an acoustic-driven atomic force microscope cantilever in liquid *Appl. Phys. Lett.* **90** 113512

[29] Landau L and Lifshitz F 1971 *Fluid Mechanics, Theoretical Physics* vol 6 (Moscow: Mir)

[30] Sader J E 1998 Frequency response of cantilever beams immersed in viscous fluids with applications to the atomic force microscope *J. Appl. Phys.* **84** 64

[31] Maali A, Hurth C, Boisgard R, Jai C, Cohen-Bouhacina T and Aime J-P 2005 Hydrodynamics of oscillating atomic force microscopy cantilevers in viscous fluids *J. Appl. Phys.* **97** 074907

[32] Sader J E and Jarvis S P 2006 Coupling of conservative and dissipative forces in frequency-modulation atomic force microscopy *Phys. Rev.* B **74** 195424

[33] Lim L T W, Wee A T S and O'Shea S J 2008 Effect of tip size on force measurement in atomic force microscopy *Langmuir* **24** 2271

[34] O'Shea S J, Welland M E and Pethica J B 1994 Atomic force microscopy of local compliance at solid—liquid interfaces *Chem. Phys. Lett.* **223** 336